Soil Dynamics and Earthquake Engineering 187 (2024) 109010

Contents lists available at ScienceDirect

Soil Dynamics and Earthquake Engineering

journal homepage: www.elsevier.com/locate/soildyn

Theoretical relationship between the horizontal-to-vertical response and Fourier spectral ratios of ground motions

Yuxin Han [a], Yan-Gang Zhao [a], Haizhong Zhang [b,*]

[a] Key Laboratory of Urban Security and Disaster Engineering of Ministry of Education, Beijing University of Technology, Beijing, 100124, China

[b] Eco-Science Course, Faculty of Agriculture, Yamagata University, 1-23, Wakaba-machi, Tsuruoka-shi, Yamagata, 997-8555, Japan

ARTICLE INFO

Keywords:
Horizontal-to-vertical response spectral ratio
Horizontal-to-vertical Fourier spectral ratio
Random vibration theory
Site effects

ABSTRACT

Similar to the horizontal-to-vertical Fourier spectral ratio (HVF) of ground motions, the horizontal-to-vertical response spectral ratio (HVR) is a valuable tool for evaluating site effects. Although these two spectral ratios often exhibit similar behaviours, each possesses its own set of properties, prompting increased attention to their relationship. Previously, the relationship between HVF and HVR has been statistically investigated to explore which is more reasonable for predominant period estimation. However, the theoretical link between them remains unexplored. To clarify their theoretical relationship, in this study, an expression relating HVR to HVF based on random vibration theory was derived. The accuracy of the derived expression was confirmed through a comparison with the results obtained via direct numerical integration using real seismic records. Subsequently, based on the derived expression, the theoretical relationship between HVF and HVR was systematically explored. HVR was found to be the result of smoothing the square of the HVF, and the spectral window for this smoothing operation was determined using the Fourier amplitude spectrum of the vertical ground motion and the oscillator transfer function.

1. Introduction

The ratio between the Fourier amplitude spectrum (FAS) of horizontal and vertical ground motions plays an important role in site effects evaluation [1]. Because the horizontal-to-vertical Fourier spectral ratio (HVF) calculation requires records from only one site without a reference station, it has garnered increased attention over the past several decades. HVF was first proposed by Lermo and Chávez-García [2] and was applied to evaluate site effects in three cities in Mexico: Oaxaca, Oax., Acapulco, Gro., and Mexico City. They [2] pointed out that if site effects are caused by simple geology, a first estimate of the predominant period and amplification level can be obtained using the HVF. Subsequently, the reliability of HVF for evaluating site effects was systematically confirmed in previous studies by comparing it with the standard spectral ratio technique [2–5]. Yamazaki and Ansary [6] confirmed the HVF stability through the attenuation relations of the velocity response spectra for the horizontal and vertical components of three damping ratios. Because of the aforementioned properties, HVF has been widely applied in earthquake engineering for various purposes [7–9]. Bayrak [10] utilized HVF to investigate the soil properties, including the predominant period, bedrock depth and the average shear wave velocity in the upper 30 m, V_{S30}. Zaré and Bard [11] employed HVF to conduct site classification based on the predominant frequency derived from HVF using strong earthquake records in Turkey. Sokolov et al. [12] utilized HVF to subdivide site class B as defined in the National Earthquake Hazards Reduction Program (NEHRP) [13]. This classification is based on the predominant frequency and shape of the amplification function derived from HVF, employing hundreds of earthquake records from Taiwan. Dimitriu et al. [14] used HVF to assess whether a site can be used as a reference station. Ghofrani et al. [15] utilized the predominant period of the HVF and V_{S30} to develop a general empirical model to reduce the depth effects in the cross-spectral ratios.

In addition, because of the well-known similarity between the acceleration FAS and the undamped velocity response spectrum [16], many studies [17–20] have utilized the response spectrum to calculate the horizontal-to-vertical spectral ratio (hereafter called HVR). As the HVR calculation does not require a smoothing procedure, as in HVF, calculating the HVR requires less effort. Therefore, Zhao et al. [21] proposed the application of HVR for site classification. Subsequently, the use of HVR to assess site effects has become increasingly widespread. Di Alessandro et al. [22], Ghofrani and Atkinson [23], and Wen et al. [24] applied HVR to site classification, enhancing the site classification

* Corresponding author.
E-mail address: zhang@tds1.tr.yamagata-u.ac.jp (H. Zhang).

https://doi.org/10.1016/j.soildyn.2024.109010
Received 5 July 2024; Received in revised form 25 September 2024; Accepted 2 October 2024

Table 1
Information of the selected sites.

Station ID	Coordinates (°)		Site conditions		Site classes	Geology properties
Code	Long.	Lat.	S (m/s)	V_{S30} (m/s)		
GIFH11	35.49	137.25	320	904.2	B	Adducts
GIFH16	36.09	137.34	200	830.8	B	Igneous rocks
AIC005	35.20	137.21	130	558.9	C	Sedimentary rocks
AIC014	34.83	137.22	180	367.5	C	Sedimentary rocks
AIC001	35.30	136.75	78	184.2	D	Sedimentary rocks
AIC004	35.06	136.97	120	334.1	D	Sedimentary rocks
AIC006	35.22	137.51	110	256.6	D	Sedimentary rocks
MYG017	37.98	140.78	80	143.9	E	Sedimentary rocks
TYM005	36.76	137.09	90	169.7	E	Sedimentary rocks
SIT011	35.81	139.72	95	152.4	E	Sedimentary rocks
AIC003	35.17	136.74	130	166.4	E	Sedimentary rocks
YMT006	38.60	140.41	70	109.9	E	Sedimentary rocks
CHB020	35.11	140.10	150	134.4	E	Sedimentary rocks
ISK014	36.30	136.32	110	133.0	E	Sedimentary rocks

techniques introduced by Zhao et al. [21]. Yaghmaei-Sabegh and Tsang [25] developed a methodology for site class mapping by adopting the HVR technique developed by Zhao et al. [21]. Fukushima et al. [26] discussed the effects of HVR site classification techniques on the development of ground-motion prediction equations (GMPEs). Hassani and Atkinson [27] as well as Yaghmaei-Sabegh and Hassani [28] proposed a V_{S30} estimation equation based on the predominant frequencies from HVR.

Although both HVF and HVR play important roles in evaluating site effects, each possesses its own set of properties. To explore which is more reasonable for predominant period estimation, the relationship between them has also garnered increased attention. Yamazaki and Ansary [6] compared HVF with HVR with a 2 % damping ratio based on 2166 three-component sets from 387 earthquakes at four sites in Japan. Dimitriu et al. [14] compared an HVF with an undamped HVR using approximately 50 earthquake records. Laouami and Slimani [29] compared HVF with HVR based on seismic records from the Algiers-Boumerdes Region. Coban [30] compared HVF with HVR using strong ground motion records from 41 stations in Bursa Province. All the aforementioned studies pointed out that HVF and HVR have a high similarity in terms of their predominant frequencies and peak spectral amplitudes. However, other studies have also pointed out discrepancies between HVF and HVR. Zhu et al. [31] compared HVF and HVR results for 207 Kiban-Kyoshin network (KiK-net) [32,33] sites in Japan. They found that the predominant frequencies derived from HVF and HVR may differ, particularly at high frequencies. They believed that HVF should be preferred because of the scenario-dependent properties of the response spectrum. Livağlu et al. [34] also found that for individual stations, the HVF and HVR results can differ, especially in sites where Fourier spectra exhibit superficial peaks at engineering bedrock, based on 485 acceleration records at 21 stations. They concluded that HVR's predominant periods revealed more reliable results for engineering purposes. Although previous studies have made significant contributions to clarifying the relationship between HVF and HVR, there are still some divergences. Moreover, all the aforementioned studies rely on statistical analyses of seismic records, and there remains a dearth of discussion regarding the theoretical relationship between HVF and HVR.

Accordingly, this study aims to clarify the theoretical relationship between HVF and HVR. The remainder of this paper is organized as follows. First, an expression relating HVR to HVF is derived based on random vibration theory (RVT) in Section 2. To confirm the accuracy of the derived expression, numerous ground motions recorded at real sites are selected in Section 3. Then, the results of the derived expression are compared with those from direct numerical integration in Section 4. Subsequently, in Section 5, the theoretical relationship between HVF and HVR is systematically explored based on the derived expression. Finally, the main conclusions of this study are summarized in Section 6.

2. Theoretical relationship between HVF and HVR

To clarify the theoretical relationship between HVF and HVR, an expression for the HVF-HVR relationship is derived in this section. According to the RVT, the response spectrum $R(\overline{\omega}, h_0)$ can be obtained from the zeroth moment of acceleration FAS of the response of a single-degree-of-freedom (SDOF) oscillator [35–38], which is expressed as

$$R(\overline{\omega}, h_0) = \frac{pf_r}{\sqrt{D_r}} \sqrt{m_{0,r}} \tag{1}$$

where $\overline{\omega}$ and h_0 are the circular frequency and damping ratio of the SDOF oscillator (hereafter referred to as the oscillator), respectively; pf_r and D_r are the peak factor and the root-mean-square oscillator response duration, respectively; and $m_{0,r}$ is the zeroth moment of the oscillator response FAS.

According to the RVT, the response spectra of the horizontal and vertical ground motions, $R_H(\overline{\omega}, h_0)$ and $R_V(\overline{\omega}, h_0)$, respectively, can be expressed as follows:

$$R_H(\overline{\omega}, h_0) = \frac{pf_{rH}}{\sqrt{D_{rH}}} \sqrt{m_{0,rH}} \tag{2}$$

$$R_V(\overline{\omega}, h_0) = \frac{pf_{rV}}{\sqrt{D_{rV}}} \sqrt{m_{0,rV}} \tag{3}$$

where pf_{rH} and pf_{rV} are the peak factors of the oscillator response for the horizontal and vertical ground motions, respectively; D_{rH} and D_{rV} are the root-mean-square oscillator response duration for the horizontal and vertical ground motions, respectively; $m_{0,rH}$ and $m_{0,rV}$ denote the zeroth spectral moments of the oscillator response for the horizontal and vertical ground motions, respectively.

The zeroth spectral moment of the horizontal ground motion oscillator response $m_{0,rH}$ can be obtained from the oscillator response FAS of the horizontal ground motion:

$$m_{0,rH} = \frac{1}{\pi} \int_0^{\infty} |A_{SH}(\omega) |H_0(\omega, \overline{\omega}, h_0)||^2 d\omega \tag{4}$$

where $A_{SH}(\omega)$ is the FAS of the horizontal ground motion, ω is the circular frequency and $H_0(\omega, \overline{\omega}, h_0)$ is the SDOF transfer function, which is expressed as

$$|H_0(\omega, \overline{\omega}, h_0)| = \frac{\overline{\omega}^2}{\sqrt{(2h_0\omega\overline{\omega})^2 + (\omega^2 - \overline{\omega}^2)^2}} \tag{5}$$

Similarly, the zeroth spectral moment of the oscillator response of the vertical ground motion $m_{0,rV}$ can be obtained from the oscillator response FAS of the vertical ground motion, as follows:

$$m_{0,rV} = \frac{1}{\pi} \int_0^{\infty} |A_{SV}(\omega) |H_0(\omega, \overline{\omega}, h_0)||^2 d\omega \tag{6}$$

where $A_{SV}(\omega)$ is the vertical ground motion FAS, which is related to the horizontal ground motion FAS:

$$A_{SH}(\omega) = A_{SV}(\omega) HVF(\omega) \tag{7}$$

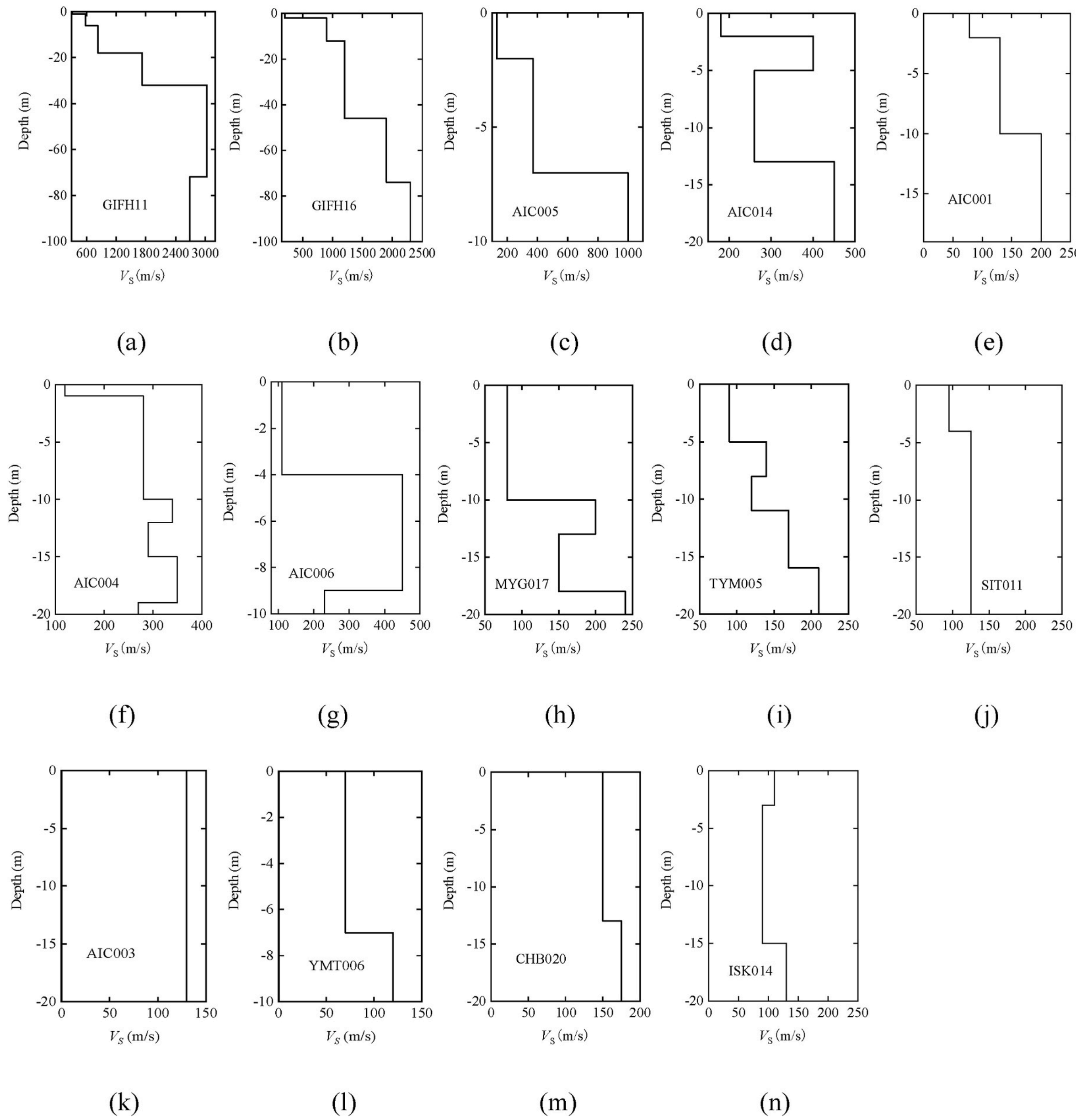

Fig. 1. Shear-wave velocity V_S profiles of the selected sites.

where $HVF(\omega)$ represents the Fourier spectral ratio of the horizontal and vertical ground motions. Therefore, HVR can be obtained by dividing $R_H(\overline{\omega},h_0)$ by $R_V(\overline{\omega},h_0)$, as follows:

$$HVR(\overline{\omega},h_0)=\frac{R_H(\overline{\omega},h_0)}{R_V(\overline{\omega},h_0)}=\sqrt{\frac{m_{0,rH}}{m_{0,rV}}}\times\frac{pf_{rH}/\sqrt{D_{rH}}}{pf_{rV}/\sqrt{D_{rV}}} \tag{8}$$

Assuming that the peak factor and root-mean-square duration of the oscillator response of the horizontal ground motion (pf_{rH}, D_{rH}) are equal to those of the oscillator response of the vertical ground motion (pf_{rV}, D_{rV}), Eq. (8) can be simplified as:

$$HVR(\overline{\omega},h_0)=\sqrt{\frac{m_{0,rH}}{m_{0,rV}}} \tag{9}$$

By substituting Eqs. (4) and (6) into Eq. (9), Eq. (9) can be rearranged as follows:

$$HVR(\overline{\omega},h_0)=\sqrt{\frac{\int_0^{\infty}W(\omega,\overline{\omega},h_0)|HVF(\omega)|^2d\omega}{\int_0^{\infty}W(\omega,\overline{\omega},h_0)d\omega}} \tag{10}$$

where $W(\omega,\overline{\omega},h_0)$ is the product of the square of the FAS of the vertical ground motion and SDOF transfer function:

$$W(\omega,\overline{\omega},h_0)=A_{SV}^2(\omega)|H_0(\omega,\overline{\omega},h_0)|^2 \tag{11}$$

For convenience, Eq. (10) is rearranged as:

$$HVR(\overline{\omega},h_0)=\sqrt{\int_0^{\infty}U_p(\omega,\overline{\omega},h_0)|HVF(\omega)|^2d\omega} \tag{12}$$

$$U_p(\omega,\overline{\omega},h_0)=\frac{W(\omega,\overline{\omega},h_0)}{\int_0^{\infty}W(\omega,\overline{\omega},h_0)d\omega} \tag{13}$$

Therefore, Eq. (10) or Eq. (12) relates HVF to HVR and can be used to explore the relationship between them.

3. Ground motion data

To verify Eq. (10) or Eq. (12) derived in Section 2, 14 sites were selected from strong-motion seismograph networks, Kyoshin net (K-

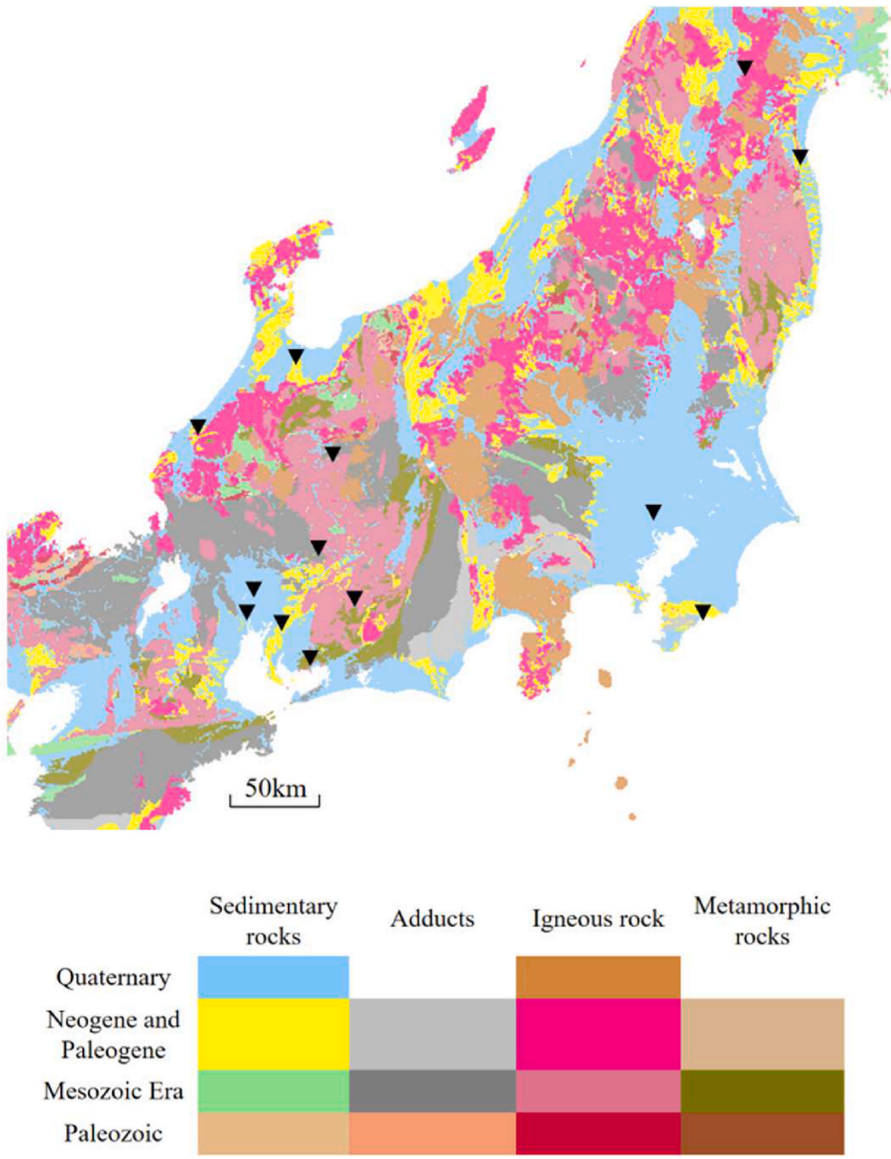

Fig. 2. Geological map of the study area, the triangles represent the selected sites.

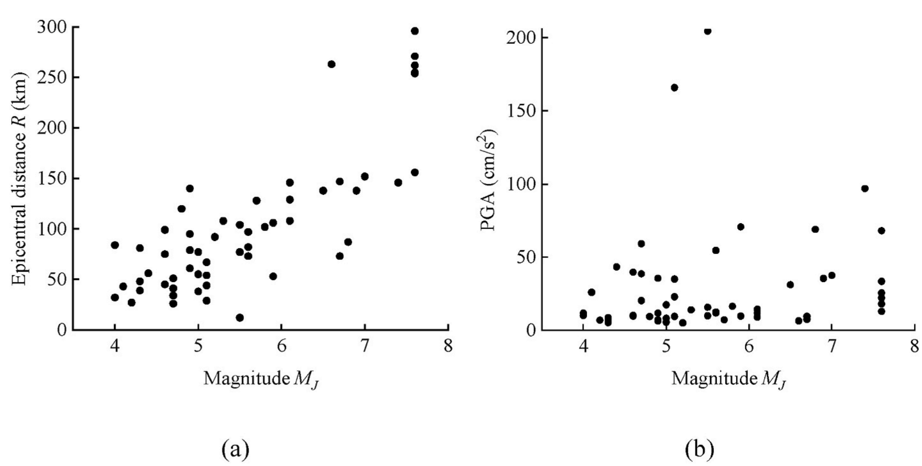

Fig. 3. Distributions of (a) magnitude M_J and epicentral distance R, and (b) magnitude M_J and PGA of the selected seismic records.

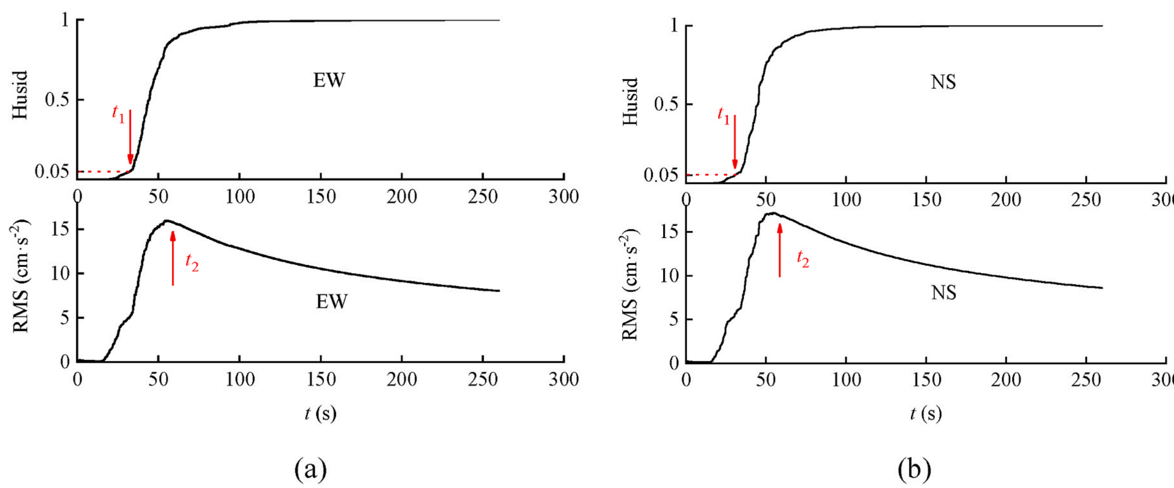

Fig. 4. Illustration of how to find the arrival time t_1 and end time t_2 of the shear wave: (a) EW component and (b) NS component. The upper figures illustrate the determination of t_1 using the Husid function, while the lower figures illustrate the determination of t_2 using the cumulative RMS function.

NET) and KiK-net [32,33], constructed by the National Research Institute for Earth Science and Disaster Prevention (NIED) [39]. Table 1 shows the information of the 14 selected sites, including the coordinates, shear wave velocity of the surface layer S, V_{S30}, site classes, and geological properties. These sites cover the four site classes (classes B, C, D, and E) defined in the NEHRP [13]. Fig. 1 shows the shear wave velocity, V_S, profiles of the selected sites and Fig. 2 presents a geological map of the study area [40], illustrating the geological properties of rocks beneath the surface soil.

In addition, four groups of seismic records were selected for each site, with each group consisting of three components: east-west (EW), north-south (NS), and vertical (V). The magnitude of these seismic records ranges from 4.0 to 7.6, the epicentral distance, R, ranges from 12 to 296 km, and the peak ground acceleration (PGA) ranges from 5.1 to 204.6 cm/s^2. Since K-NET and KiK-net only provide the Japan Meteorological Agency magnitude, M_J, this study adopts M_J. Fig. 3(a) shows the distribution of magnitude M_J and epicentral distance R, and Fig. 3(b) shows the distribution of magnitude M_J and PGA.

4. Verification of the derived relationship between HVF and HVR

Before calculating the HVF and HVR, the shear wave portion was selected from the seismic ground motion based on the methods of Husid [41] and McCann and Shah [42]. The key task in applying these methods is to determine the arrival time (t_1) and end time (t_2) of the shear wave. Fig. 4 illustrates how to find the arrival time t_1 and end time t_2 for a seismic record. The arrival time t_1 is estimated using the Husid function $H_n(t)$, expressed as $H_n(t) = \int_0^T [a(t)]^2 dt / \int_0^\infty [a(t)]^2 dt$. Here, $a(t)$ represents the acceleration time history, t represents time, and T represents the duration for integration. The time T, when $H_n(t)$ reaches 5 %, is defined as the arrival time t_1. Additionally, the end time t_2 is estimated using the cumulative root mean square (RMS) function, expressed as $RMS = \sqrt{\frac{1}{T}\int_0^T \|a(t)\|^2 dt}$. The time t_2 corresponds to the point where the cumulative RMS function starts to decrease along the time axis. Thus, the portion of the wave between t_1 and t_2 is the shear wave. Fig. 5 shows the shear wave portions obtained for the horizontal components of an example seismic record.

In addition, a baseline correction was utilized to correct the acceleration time series. The HVFs were calculated based on the FAS of the ground motion. The HVRs were then calculated from the HVFs using Eq. (10) and seismic records via direct numerical integration. Generally, HVF and HVR are obtained by dividing the square root of the product of the two horizontal components (EW and NS) by its vertical component (V). However, since Eq. (10) incorporates only one horizontal component, the EW component was used first for verification. Additionally, as the calculation of HVFs is for verifying the derived equation rather than for practical use, the FAS was not smoothed. Finally, to explore the influence of damping ratios, three damping ratios, namely, 2 %, 5 %, and 20 %, were considered in the calculations.

The HVRs obtained using Eq. (10) were compared with those obtained via direct numerical integration. Figs. 6–9 show representative results for 4 sites, belonging to site classes B, C, D, and E, respectively. For reference, unsmoothed HVF results are presented in these figures. To explore the effects of ground motion and damping ratio, each figure includes 4 groups of ground motions as well as 3 different damping ratios (2 %, 5 %, and 20 %). Firstly, the relationship between HVR and HVF can be observed in these figures. The overall shapes of the HVR curve resembled those of the unsmoothed HVF curve, with their maximum values occurring at the same period. This phenomenon is highly consistent with the statistical results of HVF and HVR in previous studies.

Figs. 6–9 show that the HVRs calculated using Eq. (10) and the direct numerical integration are very similar, regardless of the site class, ground motion, or damping ratio. Although the inconsistency between HVRs from Eq. (10) and direct numerical integration may be large in a few cases (e.g., Fig. 7(i) and (l)), the peaks and predominant frequencies

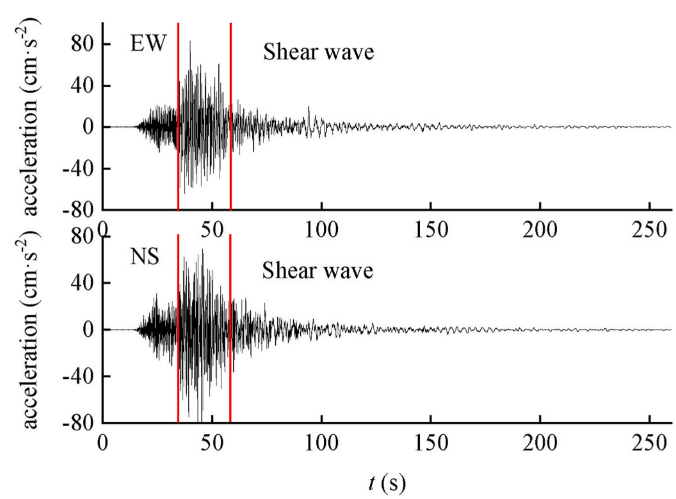

Fig. 5. The shear wave portions for the two horizontal components (EW and NS) of a seismic record.

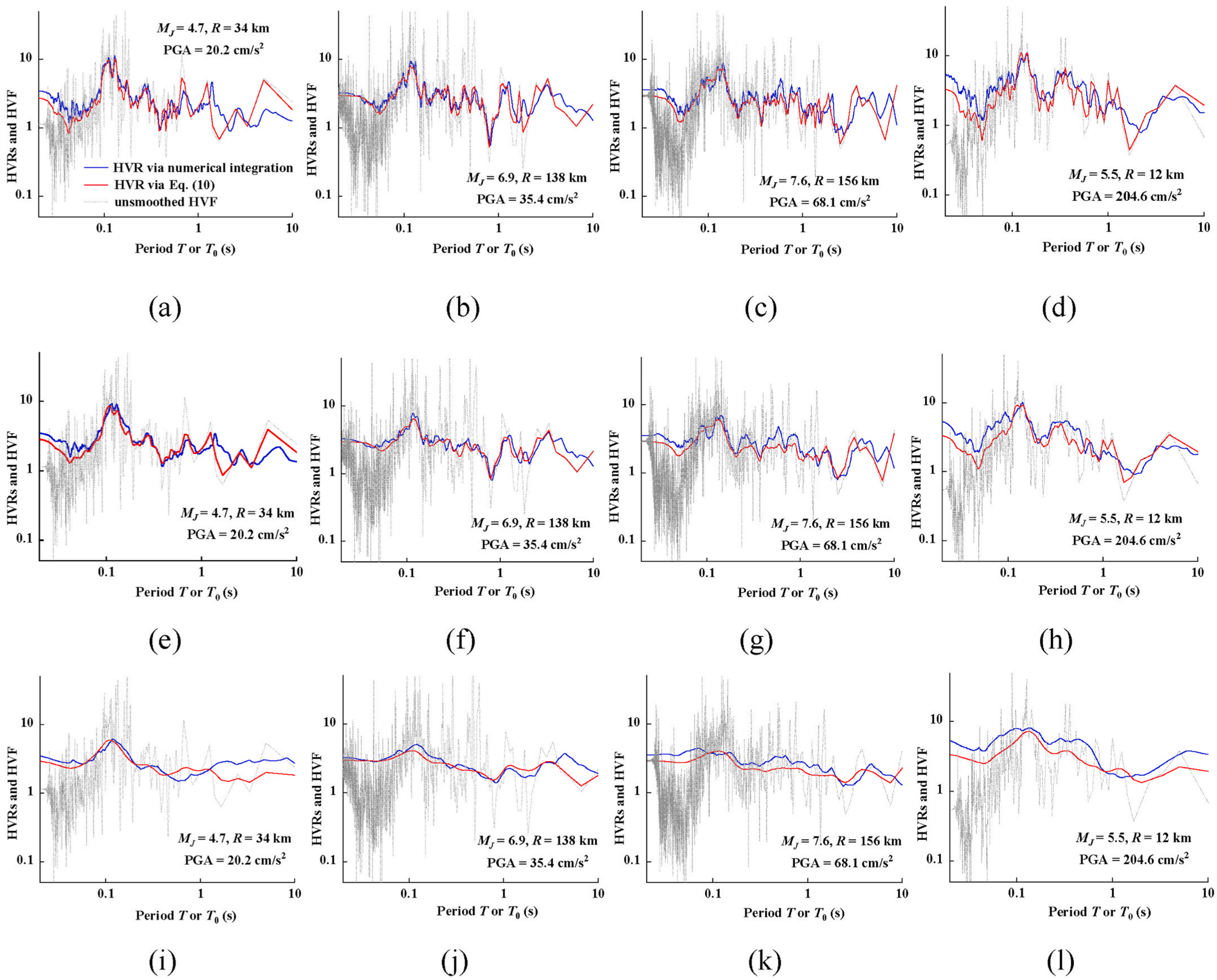

Fig. 6. Comparison of the HVR results obtained via the derived expression (Eq. (10)) and direct numerical integration for four groups of different ground motions at site GIFH16 (site class B). Each row shows the results for different damping ratios h_0: 2 %, 5 %, and 20 %, from top to bottom, respectively.

of both remain similar. In addition, by comparing results across different figures, the influence of site conditions can be observed. It is noted that although the peaks of these spectral ratios shift to longer periods as the site becomes softer, the consistency between HVRs from Eq. (10) and direct numerical integration remains unchanged. By comparing different columns in each figure, the effect of ground motion can be observed. Although the results vary with different ground motions, no consistent trends were found with changes in magnitude M_J, epicentral distance R, or PGA. The consistency between the HVRs from the two methods remains unaffected by ground motion. Moreover, by comparing different rows in each figure, the impact of the damping ratio can be observed. As the damping ratio increases, the shape of the HVR curve becomes smoother; however, this does not affect the degree of consistency between the HVRs from the two methods. The same phenomenon is observed for results not shown here, such as those for sites GIFH11, AIC014, AIC001, AIC006, MYG017, TYM005, SIT011, AIC003, CHB020, and ISK014. These results verify the accuracy of the derived equation (Eq. (10)) and also support the assumption that the peak factor and root-mean-square duration of the oscillator response of the horizontal ground motion (pf_{rH}, D_{rH}) are similar to those of the oscillator response of the vertical ground motion (pf_{rV}, D_{rV}).

The aforementioned validations of Eq. (10) are based on a single horizontal component. However, it is well known that the geometric mean of the two horizontal components (EW and NS) is typically used for the calculation of HVR and HVF. Nevertheless, since the geometric mean of the EW and NS components can be treated as a new single component, Eq. (10) remains valid for cases involving two horizontal components. This is because if the one-component FAS $A_{SH}(\omega)$ in Eqs. (4) and (7) is replaced by the geometric mean FAS of the EW and NS components, the response spectra from Eq. (2) correspond to the geometric mean of the two horizontal components. Thus, Eq. (10) can also represent the relationship between HVR and HVF considering the two horizontal components.

To verify the accuracy of Eq. (10) when incorporating two horizontal components, HVRs were calculated using Eq. (10), with HVFs obtained by dividing the geometric mean of the two horizontal components by the vertical component. The HVRs from Eq. (10) were then compared to those obtained via direct numerical integration, where the HVRs were also calculated by dividing the geometric mean of the two horizontal components by the vertical component. Fig. 10 shows the comparison for sites GIFH16, AIC005, AIC004, and YMT006. Each row corresponds to results for different ground motions, and each column presents results for different damping ratios. The results show that the HVRs calculated using Eq. (10) closely match those obtained via direct numerical

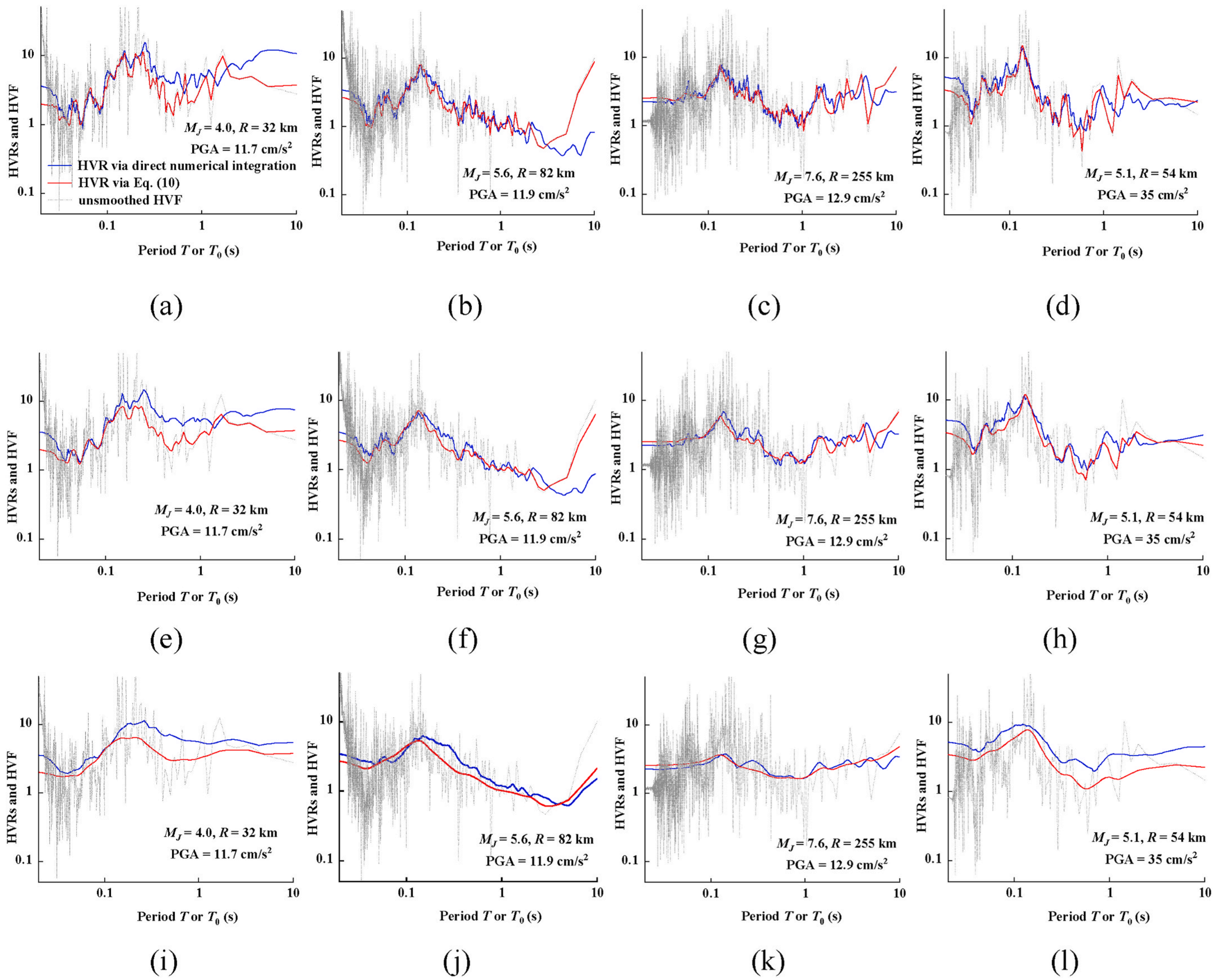

Fig. 7. Comparison of the HVR results obtained via the derived expression (Eq. (10)) and direct numerical integration for four groups of different ground motions at site AIC005 (site class C). Each row shows the results for different damping ratios h_0: 2 %, 5 %, and 20 %, from top to bottom, respectively.

integration, even when considering two horizontal components.

5. Theoretical relationship between HVR and HVF

In this section, the theoretical relationship between HVF and HVR is systematically explored based on the derived expression. Firstly, the derived expression, i.e., Eq. (12), was analyzed in detail. It is found that Eq. (12) represents the smoothing process of the function. In this context, $HVF^2(\omega)$ is a function to be smoothed, $U_p(\omega,\overline{\omega},h_0)$ is the smoothing spectral window, and $HVR(\overline{\omega},h_0)$ is the result obtained after smoothing. The term $U_p(\omega,\overline{\omega},h_0)$ satisfies the conditions required for spectral window smoothing (i.e., $\int_0^{+\infty} U_p(\omega,\overline{\omega},h_0)d\omega = 1$). Fig. 11 illustrates the smoothing process described in Eq. (12). The smoothing process for each oscillator period T_0 ($T_0 = 2\pi/\overline{\omega}$) involved a weighted average calculation, where the spectral window used for smoothing acted as a weighting function. Specifically, the $HVR(\overline{\omega},h_0)$ value at T_0 is equal to the weighted average of the $HVF^2(\omega)$ values from zero to infinity at the circular frequency ω, and the $U_p(\omega,\overline{\omega},h_0)$ value at ω represents the weight of the $HVF^2(\omega)$ values at the same circular frequency. To calculate $HVR(\overline{\omega},h_0)$ for different oscillator periods, the smoothing window $U_p(\omega,\overline{\omega},h_0)$ needs to be shifted to the target T_0. Each time the smoothing window is shifted, HVF is smoothed, resulting in an HVR value. Eventually, the HVR was constructed by connecting all points with different oscillator periods. The smoothing processes shown in Eq. (12), can be preliminarily understood by comparing the overall shapes of the HVR and unsmoothed HVF curves shown in Figs. 6–9.

To clarify the relationship between HVR and HVF based on the idea of smoothing, the characteristics of the spectral window for smoothing $U_p(\omega,\overline{\omega},h_0)$ were investigated. It is evident from Eqs. (11) and (13) that $U_p(\omega,\overline{\omega},h_0)$ is determined by the FAS of the vertical ground motion $A_{SV}(\omega)$ and oscillator transfer function $H_0(\omega,\overline{\omega},h_0)$. To illustrate their properties, representative results for $H_0(\omega,\overline{\omega},h_0)$ and $A_{SV}^2(\omega)$ are shown in Figs. 12 and 13, respectively. In Fig. 12, three oscillator periods ($T_0 =$ 0.5, 1, and 2 s) are considered with $h_0 = 5$ %. In Fig. 13, the FAS of the vertical ground motion $A_{SV}^2(\omega)$ was calculated based on the two seismic records for site YMT006. One seismic record has an M_J of 7.4 and R of 146 km, while the other has an M_J of 4.9 and R of 140 km.

As shown in Fig. 12, irrespective of the oscillator period T_0 shift, $H_0(\omega,\overline{\omega},5\%)$ has a narrow-band peak at the oscillator period T_0 and decreases rapidly to zero and unity as the period decreases and

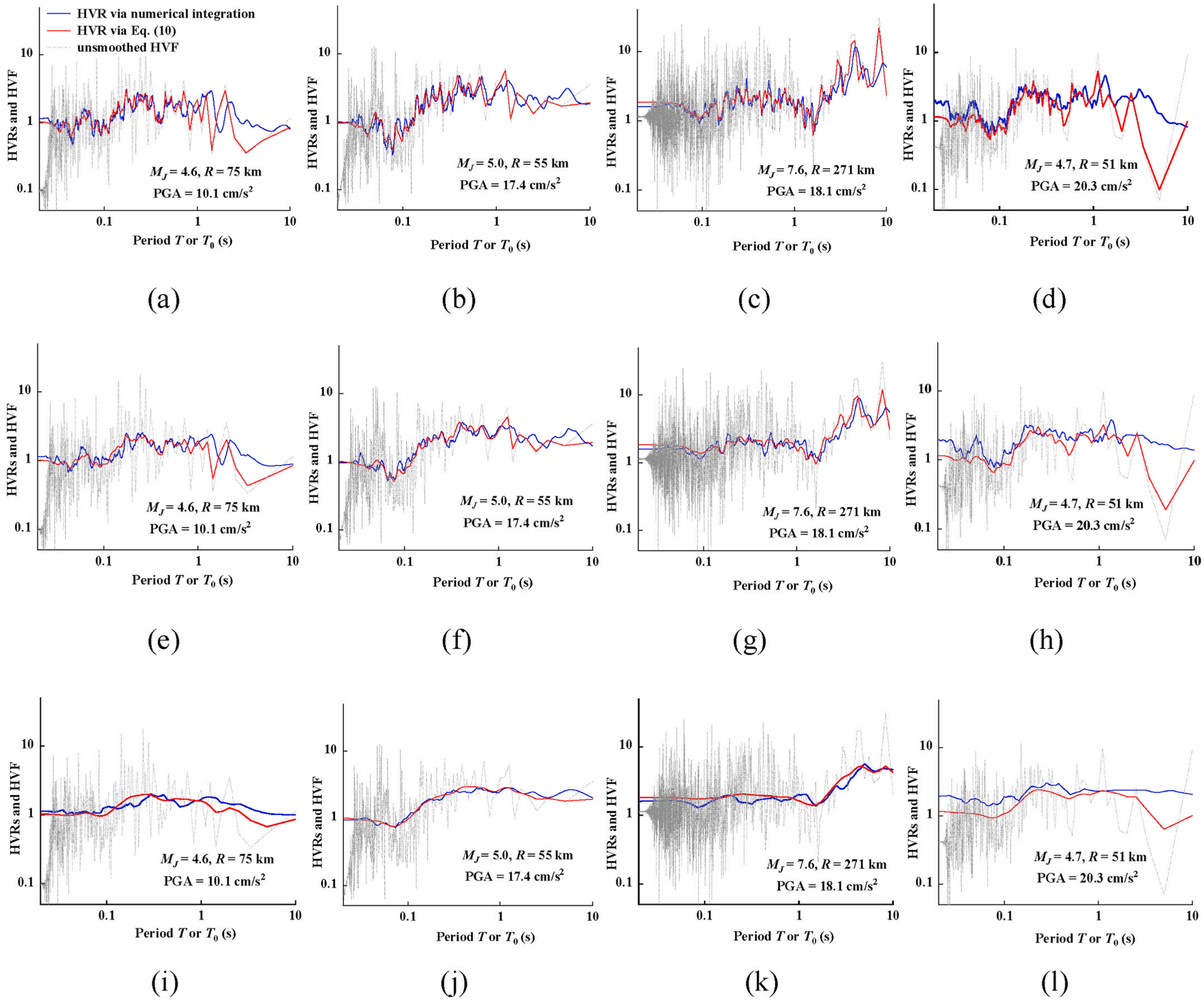

Fig. 8. Comparison of the HVR results obtained via the derived expression (Eq. (10)) and direct numerical integration for four groups of different ground motions at site AIC004 (site class D). Each row shows the results for different damping ratios h_0: 2 %, 5 %, and 20 %, from top to bottom, respectively.

increases, respectively. Fig. 13 shows that the overall shape of $A_{SV}^2(\omega)$ is much flatter than that of $H_0(\omega,\overline{\omega},5\%)$ and changes with the magnitude. When the magnitude was small ($M_J = 4.9$), $A_{SV}^2(\omega)$ exhibited an obvious peak over a short period. As the magnitude increases, the long-period components of $A_{SV}^2(\omega)$ increase relative to the short-period components, the peak becomes less obvious, and the overall shape of $A_{SV}^2(\omega)$ becomes flatter.

According to the properties of $H_0(\omega,\overline{\omega},h_0)$ and $A_{SV}^2(\omega)$, the characteristics of $U_p(\omega,\overline{\omega},h_0)$ can be understood. As indicated by Eqs. (11) and (13), $U_p(\omega,\overline{\omega},h_0)$ is expressed in the form of the product of $A_{SV}^2(\omega)$ and $|H_0(\omega,\overline{\omega},h_0)|^2$, and the shape of $U_p(\omega,\overline{\omega},h_0)$ is determined by those of $|H_0(\omega,\overline{\omega},h_0)|^2$ and $A_{SV}^2(\omega)$. Because $H_0(\omega,\overline{\omega},h_0)$ has a very sharp peak around T_0 and the overall shape of $A_{SV}^2(\omega)$ is much flatter than that of $H_0(\omega,\overline{\omega},h_0)$, $U_p(\omega,\overline{\omega},h_0)$ typically has a sharp peak around T_0. This property can be supported by Fig. 14, which presents the $U_p(\omega,\overline{\omega},5\%)$ results for various vertical ground motions and oscillator periods. This means that the spectral window weights are typically concentrated around the oscillator period T_0.

To explore the influence of the damping ratio on HVR, Fig. 15 shows the oscillator transfer function $H_0(\omega,\overline{\omega},h_0)$ under different damping ratios. It can be seen that the larger the damping ratio, the flatter $H_0(\omega,\overline{\omega},h_0)$ becomes. Because $U_p(\omega,\overline{\omega},h_0)$ is the product of $A_{SV}^2(\omega)$ and $H_0(\omega,\overline{\omega},h_0)$, as the damping ratio increases, the smoothing window $U_p(\omega,\overline{\omega},h_0)$ also becomes flatter. As shown in Fig. 16, when the damping ratio is increased from 5 % to 20 %, the smoothing window width becomes wider. Widening the smoothing window means that the bandwidth of the weight function becomes larger, which is the weight distribution of the smoothing window function becoming more dispersed, resulting in a smoother overall trend. Therefore, a higher damping ratio leads to a more pronounced smoothing effect on HVR, making the overall trend smoother. This explanation aligns well with the phenomenon observed in the discussion of the results in Section 4.

6. Conclusion

In this study, a theoretical relationship between HVF and HVR was derived based on RVT, which is expressed as $HVR(\overline{\omega},\ h_0) =$

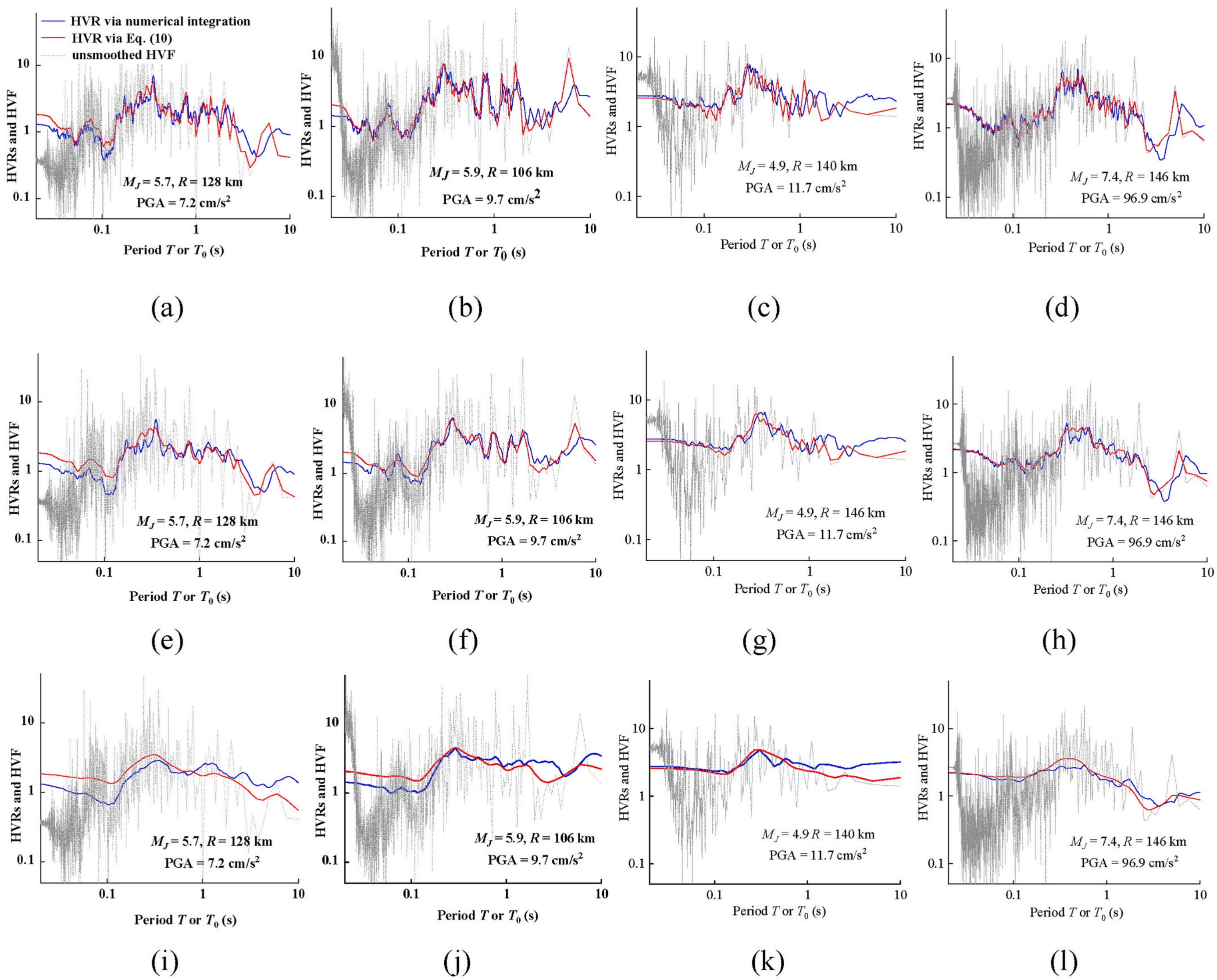

Fig. 9. Comparison of the HVR results obtained via the derived expression (Eq. (10)) and direct numerical integration for four groups of different ground motions at site YMT006 (site class E). Each row shows the results for different damping ratios h_0: 2 %, 5 %, and 20 %, from top to bottom, respectively.

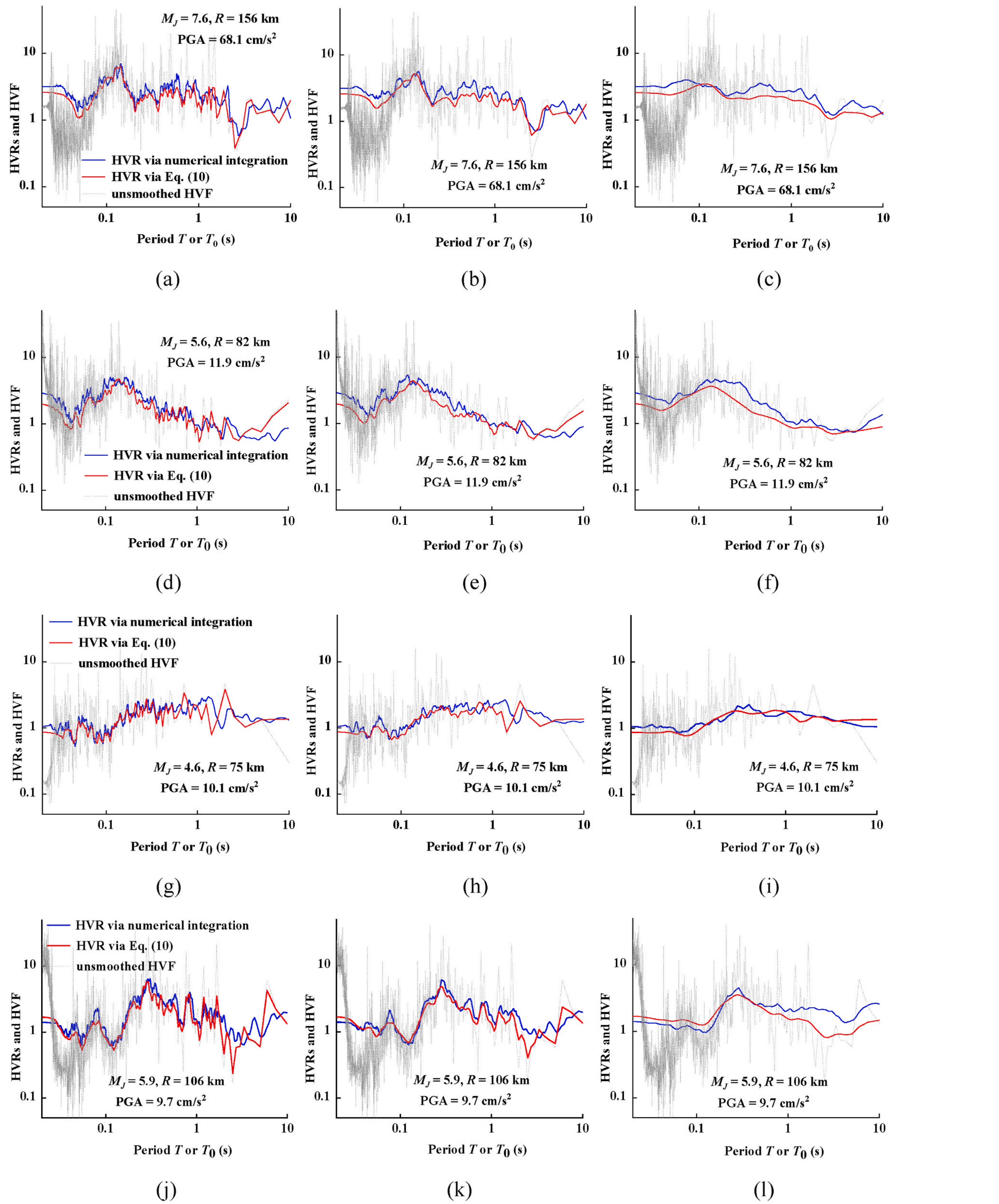

Fig. 10. Comparison of the HVR results obtained via the derived expression (Eq. (10)) using whole 3 components and direct numerical integration. Each row shows the results for different sites: GIFH16, AIC005, AIC004, and YMT006, from top to bottom, respectively. Each column shows the results for different damping ratios h_0: 2 %, 5 %, and 20 %, from left to right, respectively.

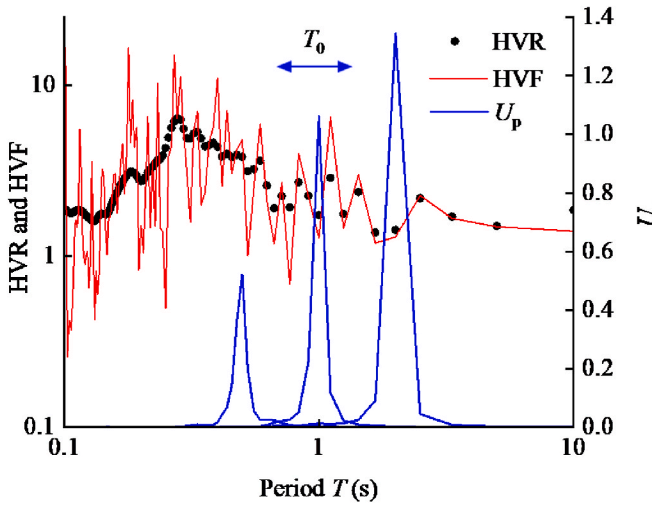

Fig. 11. Illustration of the smoothing process represented by Eq. (12).

$\sqrt{\int_0^\infty U_p(\omega, \overline{\omega}, h_0)|HVF(\omega)|^2 d\omega}$. The accuracy of the derived expression was confirmed through a comparison with the results obtained via direct numerical integration using real seismic records. Finally, the theoretical relationship between HVF and HVR was systematically explored based on the derived expressions. The main conclusions of this study can be summarized as follows:

1. HVR is the smoothed form of the square of HVF, and the spectral window for smoothing is determined by the FAS of the vertical ground motion and oscillator transfer function.
2. The overall shapes of the HVF and HVR curves are considerably similar, with their maximum values occurring at the same period.
3. As the damping ratio increases, the bandwidth of the smoothing spectral window also increases, resulting in increased smoothness. Consequently, the overall shape of both calculated HVR curves became smoother.

The above conclusions make it easier to infer the general shape of one type of spectral ratio (HVF or HVR) from the other. They can also be used to better understand the properties of observed HVR at an unknown site. Moreover, the derived theoretical expression clarifies the mathematical relationship between HVF and HVR, which may promote the application of HVR. For example, if HVR just represents a smoothed form of the square of HVF, HVR may potentially be applied in the field of microtremor, avoiding the smoothing procedure required for HVF calculations, though further work may be needed in the future.

Funding

This work was supported by the Japan Society for the Promotion of Science (JSPS) KAKENHI (Grant No. 24K17336) and the National Natural Science Foundation of China (Grant No. 52278135) and Beijing University of Technology.

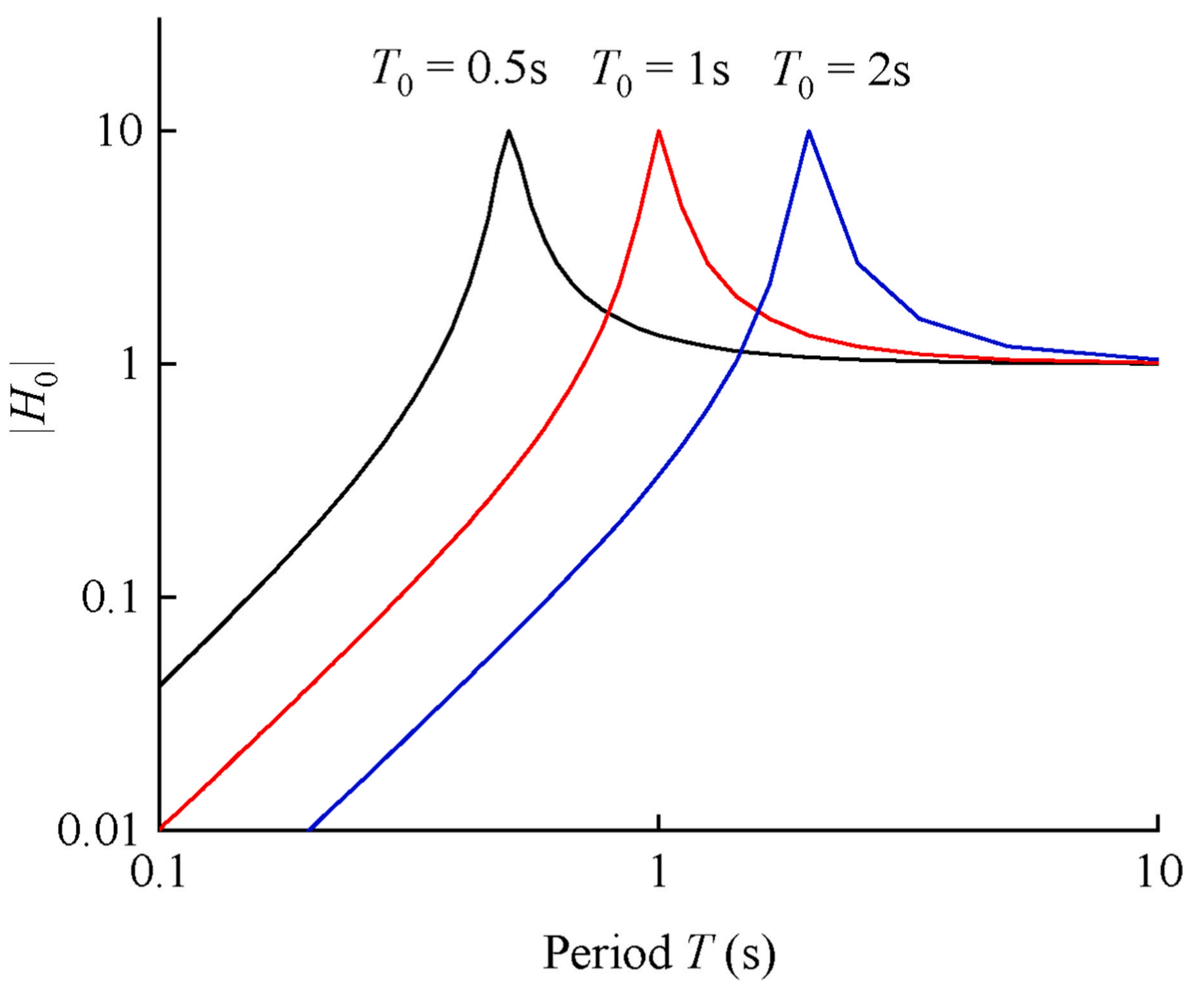

Fig. 12. Values related to the oscillator transfer function $H_0(\omega, \overline{\omega}, 5\%)$ for three different oscillator periods.

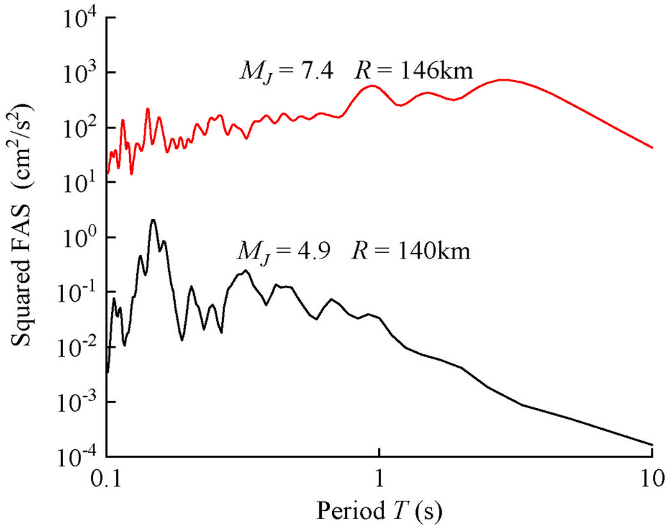

Fig. 13. Squared values of the FAS of the vertical ground motion $A_{SV}^2(\omega)$ with different magnitudes.

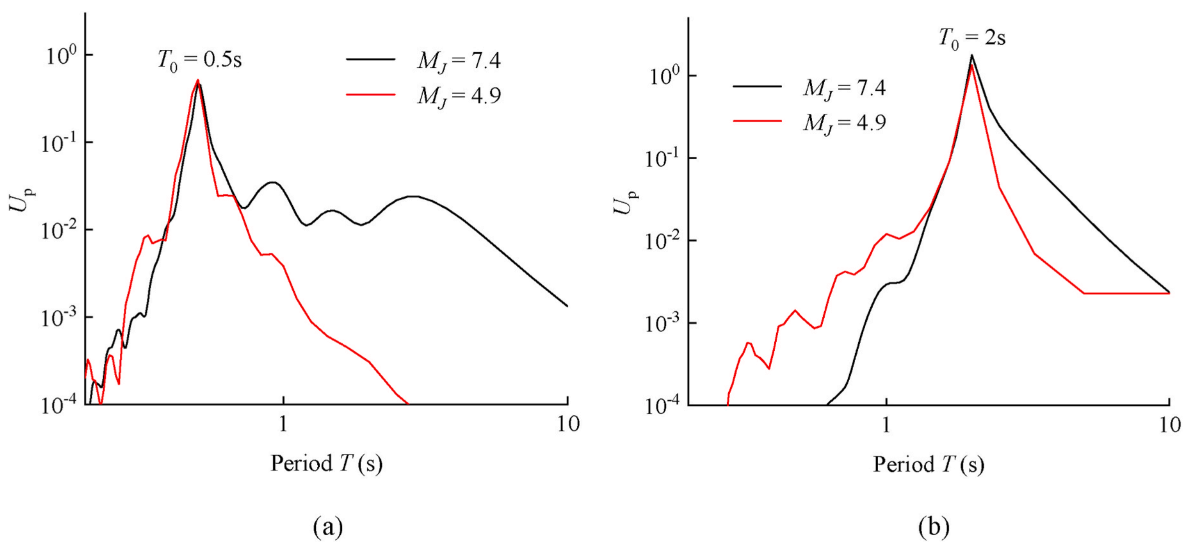

Fig. 14. Smoothing window $U_p(\omega, \overline{\omega}, 5\%)$ values for different vertical ground motion and oscillator periods: (a) $T_0 = 0.5$ s and (b) $T_0 = 2$ s.

Code availability

Available upon request.

Statement of originality

The relationship between the horizontal-to-vertical Fourier spectral ratio (HVF) and horizontal-to-vertical response spectral ratio (HVR) has been widely studied. This study reviewed the existing literature and found that previous studies primarily focused on statistical analysis and lacked a discussion of the theoretical relationship between them. In this study, an expression relating HVR to HVF based on random vibration theory was derived. The accuracy of the derived expression was confirmed through a comparison with the results obtained via direct numerical integration using real seismic records. Subsequently, based on the derived expression, the theoretical relationship between HVF and HVR was systematically explored. HVR was found to be the result of smoothing the square of the HVF, and the spectral window for this smoothing operation was determined using the Fourier amplitude spectrum of the vertical ground motion and the oscillator transfer function.

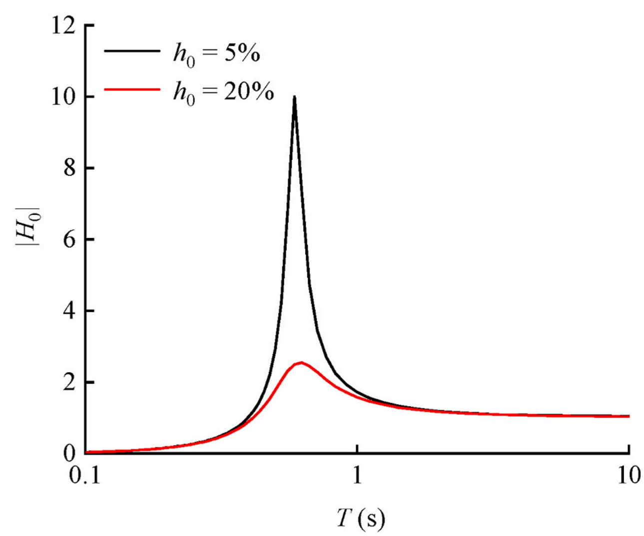

Fig. 15. Variation of the oscillator transfer function $H_0(\omega, \overline{\omega}, h_0)$ with damping ratio.

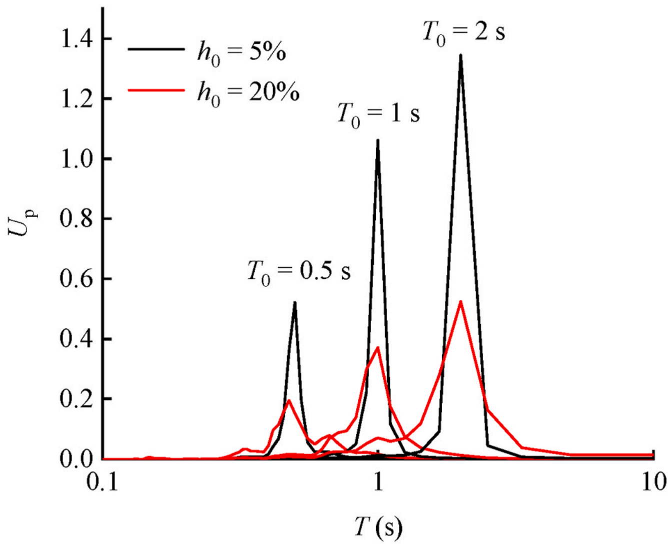

Fig. 16. Variation of the smoothing window $U_p(\omega, \overline{\omega}, h_0)$ with damping ratio for three different oscillator periods.

CRediT authorship contribution statement

Yuxin Han: Writing – original draft, Visualization, Methodology, Data curation, Conceptualization. **Yan-Gang Zhao:** Writing – review & editing, Supervision, Data curation. **Haizhong Zhang:** Writing – review & editing, Supervision, Methodology, Investigation, Conceptualization.

Declaration of competing interest

The authors declare that they have no known competing financial interests or personal relationships that could have appeared to influence the work reported in this paper.

Data availability

Data will be made available on request.

Acknowledgments

We acknowledge the support received from the Japan Society for the Promotion of Science (JSPS) KAKENHI and the National Natural Science Foundation of China and Beijing University of Technology, which were instrumental in ensuring the success of this study.

References

[1] Yaghmaei-Sabegh S. A new model to incorporate pulse-like motions effect into the FAS prediction models. Nat Hazards 2024:1–12.
[2] Lermo J, Chávez-García FJ. Site effect evaluation using spectral ratios with only one station. Bull Seismol Soc Am 1993;83(5):1574–94.
[3] Field EH, Jacob KH. A comparison and test of various site-response estimation techniques, including three that are not reference-site dependent. Bull Seismol Soc Am 1995;85:1127–43.
[4] Field EH. Spectral amplification in a sediment-filled valley exhibiting clear basin-edge-induced waves. Bull Seismol Soc Am 1996;86(4):991–1005.
[5] Theodulidis NP, Bard PY. Horizontal to vertical spectral ratio and geological conditions: an analysis of strong motion data from Greece and Taiwan (SMART-1). Soil Dynam Earthq Eng 1995;14:177–97.
[6] Yamazaki F, Ansary MA. Horizontal-to-vertical spectrum ratio of earthquake ground motion for site Characterization. Earthq Eng Struct Dynam 1997;26(7):671–89.
[7] García-Jerez A, Seivane H, Navarro M, Martínez-Segura M, Piña-Flores J. Joint analysis of Rayleigh-wave dispersion curves and diffuse-field HVSR for site characterization: the case of El Ejido town (SE Spain). Soil Dynam Earthq Eng 2019;121:102–20.
[8] Seivane H, García-Jerez A, Navarro M, Molina L, Navarro-Martínez F. On the use of the microtremor HVSR for tracking velocity changes: a case study in Campo de Dalías basin (SE Spain). Geophys J Int 2022;230(1):542–64.
[9] Karsli F, Bayrak E. Single-station microtremor surveys for site characterization: a case study in Erzurum city, eastern Turkey. Earthq Eng Eng Vib 2024;23(3):563–76.
[10] Bayrak E. Investigation of soil dynamic properties using horizontal-to-vertical spectral ratio for Eastern Pontides, Northeast Turkey. Environ Earth Sci 2022;81(21):514.
[11] Zaré M, Bard PY. Strong motion dataset of Turkey: data processing and site classification. Soil Dynam Earthq Eng 2002;22(8):703–18.
[12] Sokolov VY, Loh CH, Jean WY. Application of horizontal-to-vertical (*H/V*) Fourier spectral ratio for analysis of site effect on rock (NEHRP-class B) sites in Taiwan. Soil Dynam Earthq Eng 2007;27(4):314–23.
[13] National Earthquake Hazards Reduction Program (NEHRP). Recommended provisions for seismic regulations for new buildings and other structures. Washington, D.C: Federal Emergency Management Agency; 2000.
[14] Dimitriu PP, Papaioannou CA, Theodulidis NP. EURO-SEISTEST strong-motion array near Thessaloniki, northern Greece: a study of site effects. Bull Seismol Soc Am 1998;88(3):862–73.
[15] Ghofrani H, Atkinson GM, Goda K. Implications of the 2011 M9.0 Tohoku Japan earthquake for the treatment of site effects in large earthquakes. Bull Earthq Eng 2013;11(1):171–203.
[16] Hudson DE. Reading and interpreting strong-motion accelerograms. Earthq Eng Res Inst 1979;112:71–6.
[17] Ghasemi H, Zare M, Fukushima Y, Sinaeian F. Applying empirical methods in site classification, using response spectral ratio (*H/V*): a case study on Iranian strong motion network (ISMN). Soil Dynam Earthq Eng 2009;29(1):121–32.
[18] Wen R, Ren Y, Shi D. Improved HVSR site classification method for free-field strong motion stations validated with Wenchuan aftershock recordings. Earthq Eng Eng Vib 2011;10:325–37.
[19] Choudhury P, Chopra S, Roy KS. Site classification for strong motion stations in Gujarat, India using response spectral ratio. Soil Dynam Earthq Eng 2016;87:138–50.
[20] Chopra S, Kumar V, Choudhury P, Yadav RBS. Site classification of Indian strong motion network using response spectra ratios. J Seismol 2018;22(2):419–38.
[21] Zhao JX, Irikura K, Zhang J, Fukushima Y, Somerville PG, Asano A, et al. An empirical site-classification method for strong-motion stations in Japan using *H/V* response spectral ratio. Bull Seismol Soc Am 2006;96(3):914–25.
[22] Di Alessandro C, Bonilla LF, Boore DM, Rovelli A, Scotti O. Predominant-period site classification for response spectra prediction equations in Italy. Bull Seismol Soc Am 2012;102(2):680–95.
[23] Ghofrani H, Atkinson GM. Site condition evaluation using horizontal-to-vertical response spectral ratios of earthquakes in the NGA-West 2 and Japanese databases. Soil Dynam Earthq Eng 2014;67:30–43.
[24] Wen RZ, Ji K, Ren YF, Wang H. Site classification for strong earthquake stations in China using spectral ratio method. Chin J Rock Mech Eng 2015;34(6):1236–41.
[25] Yaghmaei-Sabegh S, Tsang HH. Site class mapping based on earthquake ground motion data recorded by regional seismographic network. Nat Hazards 2014;73:2067–87.
[26] Fukushima Y, Bonilla LF, Scotti O, Douglas J. Site classification using horizontal-to-vertical response spectral ratios and its impact when deriving empirical ground-motion prediction equations. J Earthq Eng 2007;11(5):712–24.
[27] Hassani B, Atkinson GM. Applicability of the site fundamental frequency as a V_{S30} proxy for central and eastern North America. Bull Seismol Soc Am 2016;106(2):653–64.
[28] Yaghmaei-Sabegh S, Hassani B. Investigation of the relation between V_{S30} and site characteristics of Iran based on horizontal-to-vertical spectral ratios. Soil Dynam Earthq Eng 2020;128:105899.
[29] Laouami N, Slimani A. Earthquake induced site effect in the Algiers-Boumerdes region: relation between spectral ratios higher peaks and observed damage during the May 21st Mw 6.8 Boumerdes Earthquake (Algeria). Pure Appl Geophys 2013;170:1785–801.
[30] Coban KH. Seismic site classification based on *H/V* spectral ratio from strong ground motion records: the urban areas of Bursa province. J Seismol 2024:1–24.
[31] Zhu CB, Cotton F, Pilz M. Detecting site resonant frequency using HVSR: Fourier versus response spectrum and the first versus the highest peak frequency. Bull Seismol Soc Am 2020;110(2):427–40.
[32] Okada Y, Kasahara K, Hori S, Obara K, Sekiguchi S, Fujiwara H, et al. Recent progress of seismic observation networks in Japan—hi-net, F-net, K-NET and KiK-net. Earth Planets Space 2004;56 [xv-xxviii].
[33] Aoi S, Kunugi T, Nakamura H, Fujiwara H. Deployment of new strong motion seismographs of K-NET and KiK-net. Earthquake data in engineering seismology: predictive models. Data Management and Networks; 2011. p. 167–86.
[34] Livağlu H, Şentürk E, Sertçelik F. A Comparative study of response and Fourier spectral ratios on classifying sites. Pure Appl Geophys 2021;178:1745–59.
[35] Boore DM. Stochastic simulation of high-frequency ground motions based on seismological models of the radiated spectra. Bull Seismol Soc Am 1983;73(6):1865–94.
[36] Boore DM. Simulation of ground motion using the stochastic method. Pure Appl Geophys 2003;160:635–76.
[37] Zhang HZ, Zhao YG. Analytical model for response spectral ratio considering the effect of earthquake scenarios. Bull Earthq Eng 2021;19:5285–305.

[38] Zhang HZ, Zhao YG, Ochiai T, Fang YC. Relationship between SDOF-input-energy and fourier amplitude spectral amplification ratios. Bull Seismol Soc Am 2023;113 (3):1230–47.
[39] National Research Institute for Earth Science and Disaster Resilience (NIED). Strong-motion seismograph networks. K-NET, KIK-net; 2019.
[40] Geological Survey of Japan, AIST. Seamless digital geological map of Japan V2 1: 200,000. 14 edition 2023. Legend.
[41] Husid R. Gravity effects on the earthquake response of yielding structures. Pasadena, California: California Institute of Technology; 1967.
[42] McCann MWJ, Shah HC. Determining strong-motion duration of earthquakes. Bull Seismol Soc Am 1979;69(4):1253–65.